SCIENCE CHINA
Physics, Mechanics & Astronomy

•Article•

March 2023 Vol. 66 No. 3: 237311
https://doi.org/10.1007/s11433-022-2020-5

Exploration of B-site alloying in partially reducing Pb toxicity and regulating thermodynamic stability and electronic properties of halide perovskites

Xinjiang Wang[1†], Muhammad Faizan[2†], Kun Zhou[2], Hongshuai Zou[2], Qiaoling Xu[3*], Yuhao Fu[1,2*], and Lijun Zhang[2,4]

[1] *State Key Laboratory of Superhard Materials, College of Physics, Jilin University, Changchun 130012, China;*
[2] *State Key Laboratory of Integrated Optoelectronics, Key Laboratory of Automobile Materials of MOE, College of Materials Science and Engineering, Jilin University, Changchun 130012, China;*
[3] *College of Physics and Electronic Engineering, Center for Computational Sciences, Sichuan Normal University, Chengdu 610068, China;*
[4] *International Center of Computational Method and Software, Jilin University, Changchun 130012, China*

Received July 20, 2022; accepted October 17, 2022; published online January 13, 2023

Alloying strategies provide a high degree of freedom for reducing lead toxicity, improving thermodynamic stability, and tuning the optoelectronic properties of ABX_3 halide perovskites by varying the alloying element species and their contents. Given the key role of B-site cations in contributing band edge states and modulating structure factors in halide perovskites, the partial replacement of Pb^{2+} with different B-site metal ions has been proposed. Although several experimental attempts have been made to date, the effect of B-site alloying on the stability and electronic properties of halide perovskites has not been fully explored. Herein, we take cubic $CsPbBr_3$ perovskite as the prototype material and systematically explore the effects of B-site alloying on Pb-containing perovskites. According to the presence or absence of the corresponding perovskite phase, the ten alloying elements investigated are classified into three types (i.e., Type I: Sn, Ge, Ca, Sr; Type II: Cd, Mg, Mn; Type III: Ba, Zn, Cu). Based on the first-principles calculations, we obtain the following conclusions. First, these B-site alloys will exist as disordered solid solutions rather than ordered structures at room temperature throughout the composition space. Second, the alloying of Sn and Ge enhances the thermodynamic stability of the cubic perovskite host, whereas the alloying of the other elements has no remarkable effect on the thermodynamic stability of the cubic perovskite host. Third, the underlying physical mechanism for bandgap tuning can be attributed to the atomic orbital energy mismatch or quantum confinement effect. Fourth, the alloying of different elements demonstrates the diversity in the regulation of crystal structure and electronic properties, indicating potential applications in photovoltaics and self-trapped exciton-based light-emitting applications. Our work provides theoretical guidance for using alloying strategies to reduce lead toxicity, enhance stability, and optimize the electronic properties of halide perovskites to meet the needs of optoelectronic applications.

lead-based halide perovskites, alloying, thermodynamic stability, first-principles calculations, optoelectronic applications

PACS number(s): 61.66.Dk, 71.20.Nr, 84.60.Jt

Citation: X. Wang, M. Faizan, K. Zhou, H. Zou, Q. Xu, Y. Fu, and L. Zhang, Exploration of B-site alloying in partially reducing Pb toxicity and regulating thermodynamic stability and electronic properties of halide perovskites, Sci. China-Phys. Mech. Astron. **66**, 237311 (2023), https://doi.org/10.1007/s11433-022-2020-5

*Corresponding authors (Qiaoling Xu, email: qlxu2015@gmail.com; Yuhao Fu, email: fuyuhaoy@gmail.com)
†These authors contributed equally to this work.

1 Introduction

Metal halide perovskites have attracted considerable interest as promising photovoltaic materials with excellent optoelectronic properties, including a widely tunable optical bandgap, long and balanced charge carrier diffusion length, and high charge carrier mobility [1-5]. However, their practical application still faces many challenges, including lead toxicity and poor long-term stability due to heat, light, and moisture stresses [6-8]. Alloying, i.e., partially replacing the original constituent elements with targeted ions, has been used as an effective method to tune the stability, reduce toxicity, and modulate the fundamental properties of perovskites. Because of the unique ionic structure, alloying in ABX_3 halide perovskites is easier and more diversified than in conventional semiconductors [9-11]. Generally, alloying at the A-site of perovskites uses monovalent organic/inorganic cations, such as MA^+, FA^+, Cs^+, and Rb^+. Such a combination of organic and inorganic ions with different ionic radii can effectively adjust the tolerance factor, thus, playing a vital role in improving the phase stability of perovskites. For example, the stability of the photoactive α phase of the mixed solid-state perovskite alloy $FA_{1-x}Cs_xPbI_3$ was determined to be higher than that of the pure $CsPbI_3$ perovskite [12]. Moreover, in most of the experiments, three or more cations, such as $Rb_{0.05}Cs_{0.1}FA_{0.85}PbI_3$ and $Rb_xCs_x(MA_{(1-2x)/2}FA_{(1-2x)/2})PbI_3$ perovskites, were typically used in the A-site alloying process [13,14]. The increase in entropy due to cation mixing further improves the perovskite stability [15]. Regarding B-site alloying, the toxic Pb^{2+} is usually replaced by the divalent Sn^{2+}, Ge^{2+} or trivalent Bi^{3+}, In^{3+} because of the reduced toxicity and isoelectronic configuration with Pb. Moreover, the B-site elements of halide perovskites dominate the band edge states, which largely determine the optoelectronic properties of the ABX_3 halide perovskites. For instance, Mn-doped $CsPbCl_3$ nanocrystals have been reported to ensure efficient exciton luminescence in perovskite hosts, mainly ascribed to the $^4T_1 \rightarrow {}^6A_1$ transition of Mn^{2+} [16]. Meanwhile, X-site alloying mainly involves three kinds of halogen ions, i.e., Cl^-, Br^-, and I^-. The observed energy difference between halogen p orbitals pushes the band edge to a higher or lower energies, accompanied by a band offset. Therefore, alloying at the X-site can significantly alter the bandgap, subsequently changing the optoelectronic performance [17-19].

Compared with A-site and X-site alloying, the introduction of various ions to the B-site lattice results in larger formation energies, which, to a certain extent, indicates that B-site alloying can regulate the thermodynamic stability in a wider range [15,20,21]. The replacement of Pb by B-site cations can also significantly reduce the toxicity of Pb-containing perovskites. Meanwhile, the electronic structure dominated by B-site cations will show significant changes. Currently, the equivalent alloying (Sn^{2+}, Ge^{2+}, Cd^{2+}, Mg^{2+}, Zn^{2+}, Cu^{2+}, Ba^{2+}, and Ca^{2+}, etc.) and heterovalent alloying (Bi^{3+}, Sb^{3+}, In^{3+}, Ce^{3+}, Eu^{3+}, and Yb^{3+}, etc.) of B-sites have been attracting considerable interest from the scientific community. Alloying equivalent metals, such as Sn, have produced narrow-bandgap materials. However, Sn-based perovskites have been proven to be highly unstable because of their capability to easily oxidize into their tetravalent Sn^{4+} state, resulting in significant defects and excess holes [1]. Similarly, Ge^{2+} is suggested as an attractive alternative for Pb^{2+}. However, the low electron binding energy of Ge^{2+} leads to its rapid oxidation to higher valence states, resulting in lower power conversion efficiency than Pb-based perovskite cells. Recently, Cd-rich perovskite $CsPb_{1-x}Cd_xBr_3$ has been prepared by introducing Cd^{2+} to the B-site, yielding a one-dimensional (1D) rod-shaped morphology, which can achieve a true blue-color emission with a high quantum yield of 48% [22]. Moreover, Mn^{2+} alloying has been proven to effectively stabilize the α-$CsPbI_3$ phase because of a small decrease in the lattice parameters and an increase in the cohesive energy [23]. By contrast, heterovalent doping, i.e., partially replacing Pb^{2+} with Bi^{3+}, can effectively change the Fermi level and flips the sign of majority charge carriers from p-type to n-type [24]. If established in hybrid perovskites, then it could enable the fabrication of devices based on a p-n perovskite homojunction with minimal lattice mismatch. Furthermore, the incorporation of heterovalent cations in halide perovskites could potentially extend their spectral range to longer wavelengths [24].

To date, several theoretical works have explored the doping or alloying of perovskite B-sites with different metal elements [25-28]. However, most of these studies do not consider the spin-orbit coupling (SOC) effect in the calculation process, which has been shown to considerably impact the electronic properties of Pb-containing perovskites. Most of the previous studies are also based on the replacement of one or a few atoms in an ordered unit cell with a small number of atoms to achieve doping concentration, which is largely due to the tractability of using small unit cells of the perovskite system for computational modeling. However, in this work, the B-site alloys of halide perovskites are observed to have disordered lattices. Therefore, proper lattice expansion is required to simulate the disordered state of B-site atoms accurately. Moreover, to our knowledge, no theoretical work currently explains the occurrence of phase transitions with changes in alloying concentrations. For example, with the increase in alloy ratio, α-$CsPbBr_3$-alloyed Cd, Mg, and Mn will show the transformation from cubic phase to hexagonal phase.

Herein, we take $CsPbBr_3$ as the prototype material to investigate the effect of B-site alloying on the stability and electronic properties of halide perovskites. We divide the ten alloying elements into three types based on the presence or

absence of the corresponding perovskite phase (i.e., Type I: Sn, Ge, Ca, Sr; Type II: Cd, Mg, Mn; Type III: Ba, Zn, Cu). We first demonstrate that all of these alloys will exist as disordered solid solutions at room temperature, in which the alloying of Sn and Ge can significantly improve the thermodynamic stability of cubic $CsPbBr_3$ perovskite. Electronic property analysis shows that the bandgap decrease of Sn alloys is due to the energy mismatch between Sn-5s/5p and Pb-6s/6p orbitals, whereas the bandgap increase of alloyed Cd, Mg, Ba, and Zn perovskites is due to the upshift of the conduction band minimum (CBM) and the downshift of the valence band maximum (VBM) because of the quantum confinement effect. We note that different types of alloys exhibit significant differences in bandgaps, effective masses, and band edge charge distributions, indicating potential applications in photovoltaics and self-trapped exciton-based light-emitting applications.

2 Results and discussion

2.1 Ground state configuration

For alloyed perovskites, the atomic arrangements at alloy sites need to be explored, which will determine the rational construction of alloy models and the calculation of electronic properties. The cluster expansion (CE) method can efficiently evaluate the relative stabilities of 10^5 structures of alloy perovskites across the range of x ($0 < x < 1$) using a low-cost computational method [29-31]. Through the CE prediction and iterative process, we can rapidly capture the ground state configurations corresponding to different component concentrations. Furthermore, we can determine whether the alloy is in an ordered configuration or a disordered solid solution from the formation energy range of the ground state structure. However, this method is usually applied in the case of a single-phase alloy, and no phase transition occurs. Thus, this method is unsuitable for Type II and Type III alloys. Here we select Sn and Ge from Type I alloys to explore the structural characteristics of $CsPb_{1-x}Sn_xBr_3$ and $CsPb_{1-x}Ge_xBr_3$ using the CE method. We explored the phase diagrams of $CsPb_{1-x}Cd_xBr_3$ and $CsPb_{1-x}Mg_xBr_3$ perovskites for Type II alloys by searching all possible structures with 60 atoms, including nine alloy ratios (x = 1/6, 1/5, …, 4/5, 5/6), involving thousands of structures to perform high-throughput first-principles calculations. For Type III alloys, we failed to identify the structures of $CsBaBr_3$, $CsZnBr_3$, and $CsCuBr_3$ in the perovskite phase in previous experimental works and the ICSD database. However, based on the existing reports, we believe that these alloyed systems still have the same cubic structure as the parent $CsPbBr_3$ when doped at low concentrations, i.e., having disordered atomic arrangements at the alloying sites [32,33].

As shown in Figure 1(a) and (b), through an expanded structure search in the entire component variation range, the formation enthalpies of $CsPb_{1-x}Ge_xBr_3$ and $CsPb_{1-x}Sn_xBr_3$ are positive and detected near the decomposition line. No phase stability conditions are observed, i.e., with significantly negative ΔH. This indicates that Sn and Ge alloys will exist in a disordered solid solution state throughout the composition space. For Type II alloys, Figure 1(c) and (d) shows that the formation enthalpy of cubic structure is smaller than that of hexagonal structure at low Cd/Mg content ($x \leqslant 0.20$), indicating that $CsPb_{1-x}Cd_xBr_3$ and $CsPb_{1-x}Mg_xBr_3$ perovskite alloys will adopt the 3D cubic structure to maintain structural stability. When the Cd/Mg content increases, the formation enthalpy of the 1D hexagonal phase decreases gradually, indicating the conversion from a 3D cubic structure to a 1D hexagonal structure. For $x > 0.85$, the formation enthalpy of the hexagonal structure is 0.1 eV/f.u. smaller than that of the cubic structure. This indicates that the $CsPb_{1-x}Cd_xBr_3$ and $CsPb_{1-x}Mg_xBr_3$ perovskites would tend to form a 1D hexagonal crystallographic structure at Cd/Mg-rich conditions. Meanwhile, Figure 1(c) shows that the ground state of $CsPb_{0.8}Cd_{0.2}Br_3$ (x = 0.2) has weak thermodynamic stability with a formation enthalpy of −0.02 eV/f.u. at T = 0 K. Notably, the thermal excitation energy at 300 K is approximately 25 meV/atom, which is larger than the negative enthalpy value [34]. This indicates that the B-site atoms should be disordered in the $CsPb_{0.8}Cd_{0.2}Br_3$ alloy structure at room temperature. Our results show that all three types of perovskite alloys exhibit disordered solid solution miscibility at room temperature.

2.2 Composition-stability relationship

We next constructed the disordered perovskite alloy structures using the special quasi-random structures approach and explored the effect of B-site alloying on thermodynamic stability [35,36]. As shown in Figure 2(a), the cubic $CsPb_{1-x}M_xBr_3$ alloy has a three-dimensional (3D) periodic structure, where the $[PbBr_6]$ and $[MBr_6]$ octahedra are randomly distributed around the Cs atoms. To assess the thermal stability, we calculated the formation energies (E_f) of $CsPb_{1-x}M_xBr_3$ with respect to their binary phases (i.e., CsBr, $PbBr_2$, and MBr_2). For Type I alloys (Figure 2(b)), the formation energies of Sn and Ge alloys decrease linearly with the increase in concentration, indicating that the addition of Sn and Ge enhances the stability of $CsPbBr_3$ cubic perovskite. With the incorporation of Ca, the formation energies of the alloys do not change significantly in most contents (from 0 to 0.75), indicating that the stabilizing effect of the optimized tolerance factor just counteracts the destabilizing effect of metastable $[CaBr_6]$ octahedra. Sr alloying increases the formation energy, showing that the stability of the cubic phase $CsPb_{1-x}Sr_xBr_3$ gradually decreases. However, negative formation energies indicate that these alloys can still be

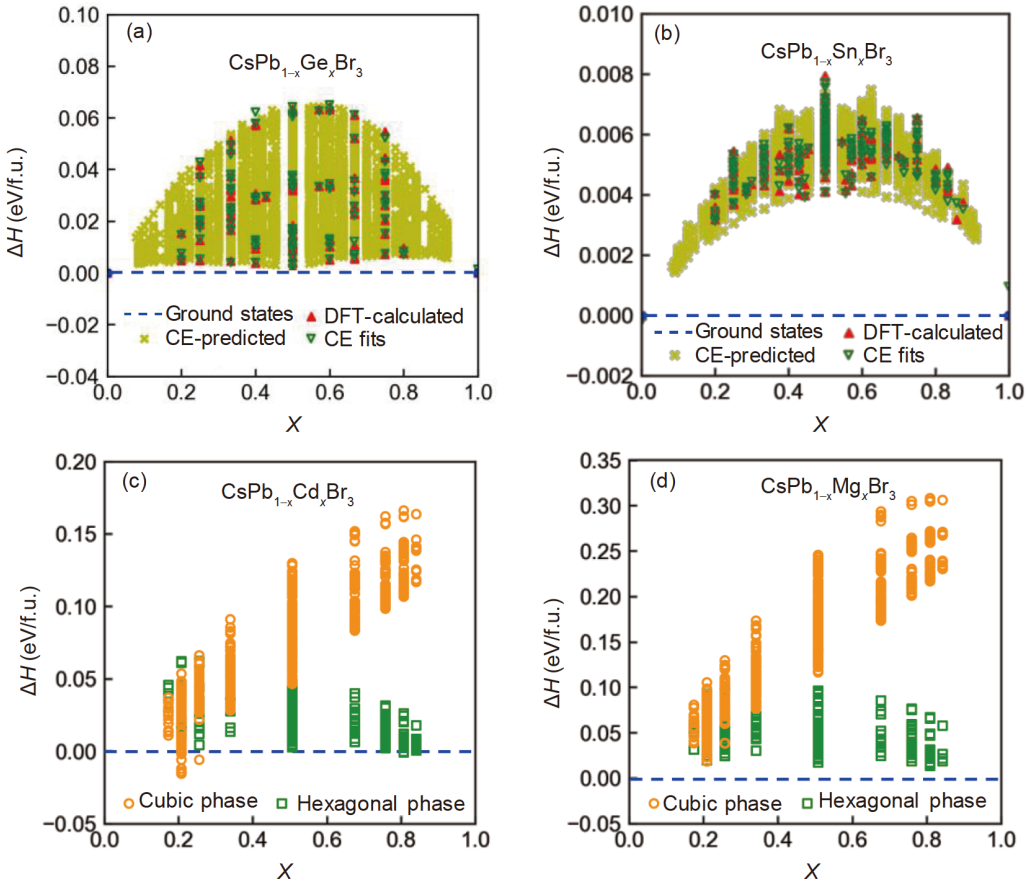

Figure 1 (Color online) Calculated formation enthalpies of the alloyed perovskites $CsPb_{1-x}M_xBr_3$ (M = Ge (a), Sn (b), Cd (c), Mg (d)) in the range of x ($0 \leqslant x \leqslant 1$). In (a) and (b), the alloy structures were generated by the CE method with the constraint of up to 20 atoms per unit cell. The red triangles denote the structures calculated by DFT, and the blue horizontal line denotes the stable ground states.

prepared experimentally. The trends of the formation energies of Type I alloys are mainly attributed to the ionic radius mismatch and the obvious difference in electron affinity between Pb^{2+} and Sn^{2+}, Ge^{2+}, Ca^{2+}, and Sr^{2+} cations. Meanwhile, the close s, p orbital energies of Pb, Sn, and Ge lead to strong band edge antibonding coupling, which reduces the total energy. Thus, Sn-alloyed and Ge-alloyed perovskites show enhanced stability. For Type II alloys (Figure 2(c)), the formation energies of cubic structures are lower than that of hexagonal structures at low contents of 0-0.125. With the increase in the content x, the total energy of the hexagonal phase gradually increases, indicating that the ground state structures of the alloys will have a more stable hexagonal configuration in the concentration range of 0.125-1. Figure 2(d) shows the variation of the formation energy for x in the range of 0-0.5 for Type III alloys. Notably, Type III alloys no longer exist in the cubic phase at higher contents. The plot shows that the formation energies increase significantly with the increase in the content x, indicating that Ba, Zn, and Cu alloying will considerably reduce the stability of cubic $CsPbBr_3$ perovskite.

2.3 Electronic properties

We selected two representative materials from each of the three types of alloys and explored the effect of alloying on their electronic properties. Here we show the electronic structure changes at two concentrations, i.e., x = 0.125 and 0.5. Many previous experimental studies have demonstrated that the maximum doping concentration of alloyed perovskites can reach 50% or even higher [22,37,38]. Figure 3 shows the effective band structures of the six alloyed perovskites with SOC effect under the Perdew-Burke-Ernzerhof (PBE) functional. The partial density of states is given in Figure S1. As shown in Figure 3(a) and (b), Sn and Ge alloys retain the electronic band characteristics of cubic phase $CsPbBr_3$ at contents of 0.125 and 0.5, showing a direct bandgap at the R point. Cd and Mg alloys also show direct bandgaps at x = 0.125 (Figure 3(c) and (d)). However, when x = 0.5, the positions of CBM and VBM shift significantly because of the transition from the cubic phase to the hexagonal phase. At the same time, the band structure shows flat band edges, indicating a significant increase in the effective

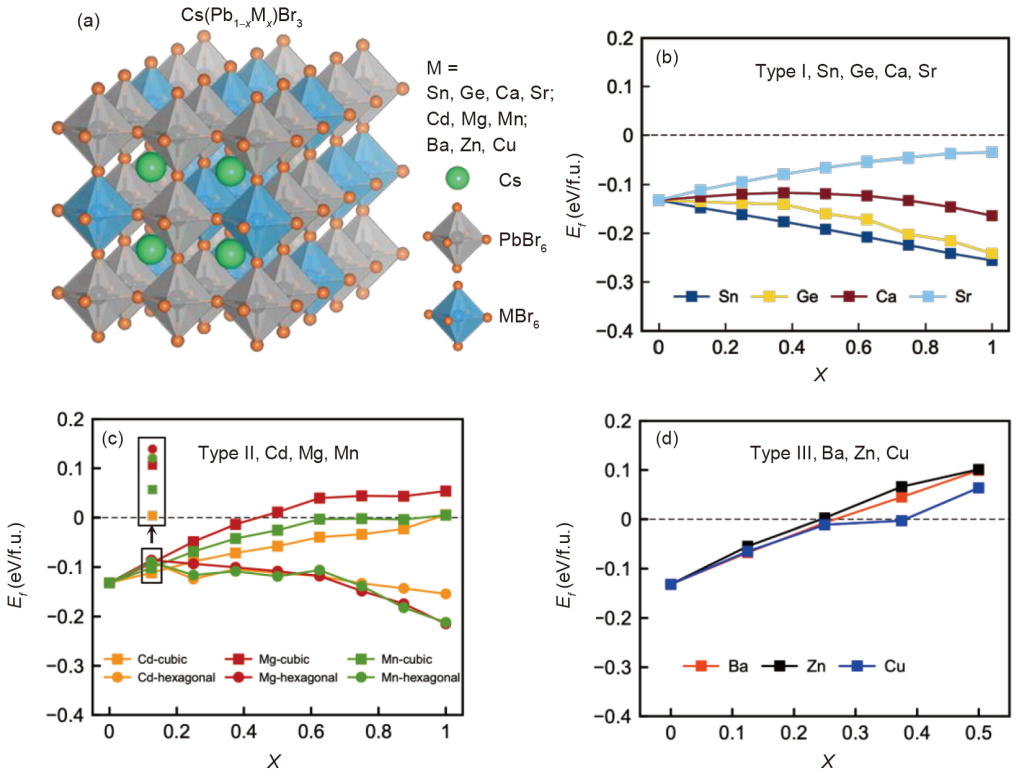

Figure 2 (Color online) (a) Schematic representation of the crystal structure of the alloyed perovskites $CsPb_{1-x}M_xBr_3$. Calculated formation energies of Type I (b), Type II (c), and Type III (d) alloys as a function of concentration.

masses of electrons and holes. Ba and Zn alloys show a direct bandgap at the R point at low contents, as shown in Figure 3(e) and (f), respectively. With the increase in the content x, the lowest unoccupied energy level of $CsPb_{0.5}Zn_{0.5}Br_3$ splits, showing a transition from a direct bandgap to an indirect bandgap.

We further explore the bandgap variation trend and the underlying physical mechanism, as shown in Figure 4(a). The bandgaps show a linear decrease (increase) for Sn and Ge (Ba and Zn) alloys with cubic structure. Meanwhile, for Cd and Mg alloys, the nonlinear change in the bandgaps was caused by the cubic-to-hexagonal phase transition (as shown in Figure S3). Specifically, the bandgaps of $CsPb_{1-x}Sn_xBr_3$ decreased from the initial value of 0.70 eV (at x = 0) to 0.38 eV (x = 0.5), whereas the bandgaps of $CsPb_{1-x}Ge_xBr_3$ remained unchanged (the bandgap of $CsPb_{0.5}Ge_{0.5}Br_3$ is 0.69 eV). The bandgaps of Cd and Mg alloys increase rapidly (up to 2.02 eV when the content x varies from 0 to 0.5). Similarly, the bandgaps of Ba and Zn alloys increased significantly, with values up to 1.2 and 0.7 eV, respectively. Such a wide bandgap range is beneficial to the application of $CsPb_{1-x}M_xBr_3$ (M = Cd, Mg, Ba, Zn) alloy perovskite systems in various fields, such as solar cells, light-emitting diodes, and radiation detectors.

Generally, decreasing the lattice constant results in an increase in the overlap between B-site and X-site atomic orbitals in ABX_3 halide perovskites. Because of the strong hybridization between B-site and X-site atomic orbitals, the VBM raises higher in energy, leading to a decrease in the bandgap. For the $CsPb_{1-x}Ge_xBr_3$ alloy, the reduction in lattice constant did not lead to a significant change in the bandgaps. To explore the physical origin of bandgap variation, we calculated the band alignment based on the average electrostatic potential, which has been reported to be used in perovskite alloy systems [39]. Figure S4 shows a nearly uniform jump in the average electrostatic potentials around the cores of atoms of the same kind, including Cs and Br. Thus, it is reasonable to align the electronic energies of different calculations by treating this uniform jump as the offset between absolute reference energies. Meanwhile, band alignment based on the deep energy levels (Cs-1s and Br-1s) confirms the rationality of the average electrostatic potential method. The band edge positions obtained by the two methods are nearly the same, except for a slight difference in the Ge and Zn alloys, as shown in Figure S5.

Figure 4(d) shows that both the CBM and VBM of Sn and Ge alloys shift upward as the increase in alloying content. The difference is that, for Sn alloys, the upshift of VBM is significantly larger than that of CBM, which leads to the reduction of the bandgaps of Sn alloys. However, the CBM and VBM of the Ge alloy exhibit a small and similar upshift. Thus, the bandgaps of Ge alloys do not change significantly. From orbital hybridization, we determine that the VBM of $CsPb_{1-x}Sn_xBr_3$ mainly comes from the antibonding states of

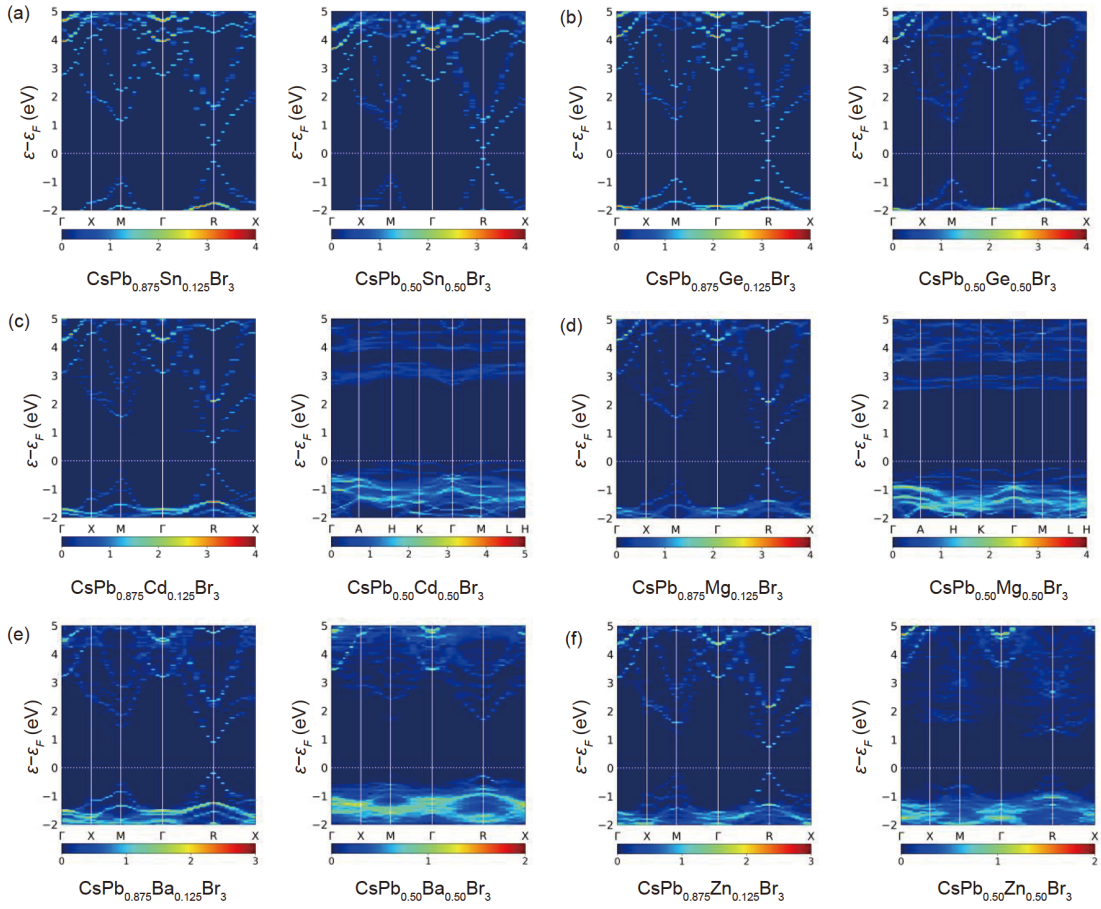

Figure 3 (Color online) Unfolded electronic band structures of $CsPb_{1-x}M_xBr_3$ perovskites, M = Sn (a), Ge (b), Cd (c), Mg (d), Ba (e), and Zn (f), and x = 0.125 and 0.5.

Sn-5s and Br-4p orbitals, and the CBM is made of the antibonding states of Sn-5p and Br-4p orbitals (Figure 4(b)). Given that the Sn-5s (5p) orbitals have higher energy than the Pb-6s (6p) orbitals, the band edge of $CsPb_{1-x}Sn_xBr_3$ is pushed up with the increase in x. However, the energy difference between Sn-5s and Pb-6s orbitals is larger than that between Sn-5p and Pb-6p orbitals, resulting in a faster increase in VBM than CBM. Thus, the bandgap of $CsPb_{1-x}Sn_xBr_3$ decreases with the increase in x. For Ge alloying, given that the energy difference between the s orbitals of Ge and Pb is nearly equal to the energy difference between their p orbitals, the upshifts of CBM and VBM are the same. Thus, the bandgaps of Ge alloys remain unchanged. Furthermore, for Cd, Mg, Ba, and Zn alloying, the bandgap increase is due to the downshift of VBM and the upshift of CBM. This Type-I-like band alignment is the result of the quantum confinement effects (Figure 4(c)). As the content x increases, the $[PbBr_6]$ octahedra with small bandgap gradually decrease and are surrounded by more $[MBr_6]$ octahedra with large bandgap. Notably, Type-I-like band alignment formed by matching the large-bandgap material with the small-bandgap material will drive the photo-generated excitons into the narrower-bandgap regions. Such regions could become light-emitting centers with a high photoluminescence quantum yield. Given that the bandgaps of the alloys can be tuned significantly by varying the concentration x, the color of emitted light can be finely adjusted, making a broadband emission profile.

Figure 5 shows the evaluation of the carrier effective masses of the alloys. The effective masses of electrons have the same increase trend as that of holes. Type I alloys (Sn/Ge) have small effective masses ($<0.2m_0$), Type III alloys (Ba/Zn) have effective masses close to $1m_0$, and Type II alloys (Cd/Mg) have large effective masses. Types I and III alloys have 3D cubic structures, whereas Type II alloys have 1D hexagonal structures at the content $x = 0.5$. Because of the discontinuous lattice structure and quantum confinement effect, the orbital wave functions between B-site atoms in the hexagonal phase have less orbital overlap in space and energy, resulting in a small band dispersion (as shown in the right panel of Figure 3(c) and (d)). Flat band edge states result in large electron/hole effective masses. Meanwhile, in cubic phase alloys, particularly Sn and Ge alloys, the 3D continuity of electronic dimensions is unbroken, thus, the

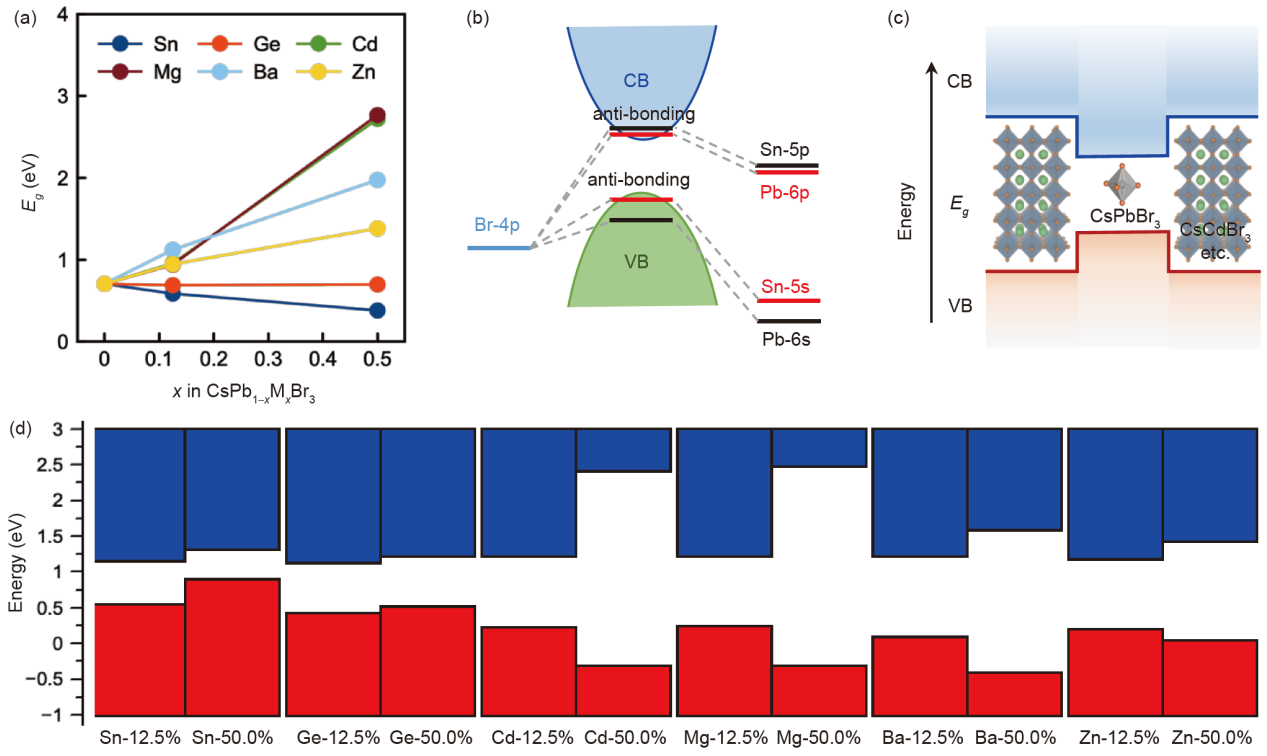

Figure 4 (Color online) (a) Calculated bandgaps using the GGA-PBE with SOC effect, the bandgap curves of Cd and Mg alloys have a high degree of overlap because of the similar bandgap values; (b) schematic diagram depicting the orbital compositions of VBM and CBM for $CsPb_{1-x}Sn_xBr_3$; (c) schematic diagram of the quantum confinement effect; (d) band alignments of $CsPb_{1-x}M_xBr_3$ (M = Sn, Ge, Cd, Mg, Ba, Zn) with x = 0.125 and 0.5.

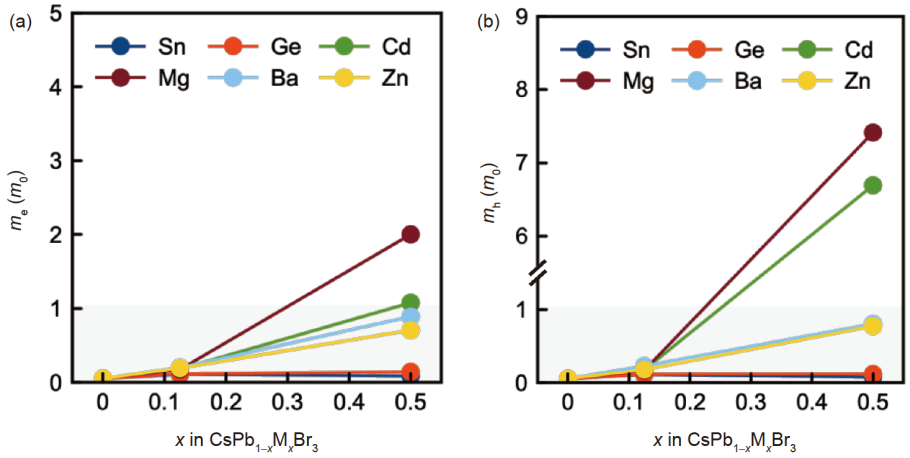

Figure 5 (Color online) Calculated effective masses of electrons (a) and holes (b) in $CsPb_{1-x}M_xBr_3$ (M = Sn, Ge, Cd, Mg, Ba, Zn). The shaded area denotes effective masses less than $1m_0$.

effective masses are smaller. Our calculated direction-dependent effective masses are given in Table S1, supporting the aforementioned conclusions. For the hexagonal Cd and Mg alloys at x = 0.5, the effective masses of electrons and holes in different directions are generally larger than those of the other cubic structure compounds.

The analysis of the band edge charge densities is helpful in thoroughly understanding the orbital contribution of the band edge states and the spatial distribution of charges. This will further motivate researchers to apply the alloyed perovskites to carrier-transport-based photovoltaic devices or self-trapped exciton-based light-emitting devices. Figure 6 shows the partial charge distribution patterns of the three types of alloys, namely, Sn, Cd, and Ba. The VBM of Sn alloys is mainly contributed by the Sn-5s and Br-4p orbitals, with a minor contribution from the Pb-6s orbitals. Pb-6p orbitals dominate the CBM with additional contributions from Sn-5p orbitals. As the content x increases, the band edge charge distribution of Sn alloys does not change significantly, as shown in Figure 6(a). The 3D connectivity of the electronic

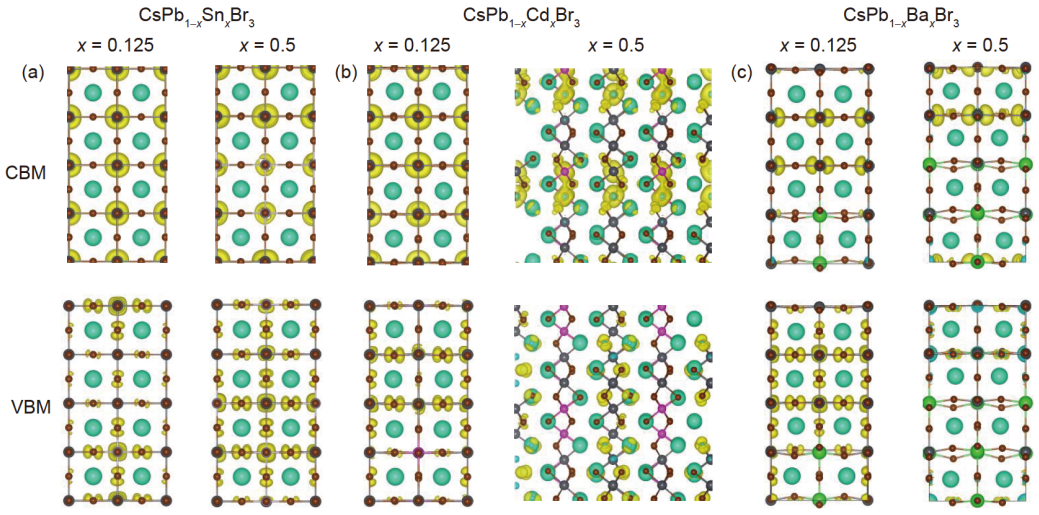

Figure 6 (Color online) Calculated partial charge distribution patterns of band edge states for the alloyed perovskites $CsPb_{1-x}M_xBr_3$, M = Sn (a), Cd (b), Ba (c). The SOC effect is included in the calculations. The isosurface level was set at 10^{-7} e/Å^3.

dimension ensures that the Sn alloy has a small effective carrier mass. For the Cd and Ba alloys, the atomic orbitals of Cd and Ba hardly contribute to the band edges. At VBM, electrons are mainly concentrated around Pb and Br, whereas at CBM, electrons are distributed around the Pb atoms, forming a local potential-well-like structure. Meanwhile, the local potential well becomes more localized with the decrease in Pb concentration. This structure resembles a conventional 2D perovskite-quantum-well structure with large exciton binding energy and high quantum yield [40-42]. At the same time, the bandgap values can be tuned by varying the concentration, which further changes the luminescence characteristics of alloyed perovskites. Notably, the SOC effect may split the conduction band edge and induce a change in the Pb orbital wavefunction. Thus, the shape of the electron cloud at the Pb-p orbital-dominated CBM after considering the SOC effect is different from that of the PBE results (as shown in Figure S6).

3 Conclusions

In this work, we explore the effect of B-site alloying on reducing Pb toxicity, improving stability, and tuning the optoelectronic properties of Pb-containing perovskite by considering ten experimentally common alloying elements. The results obtained using CE methods combined with high-throughput calculations indicate that the weak bonding of perovskite B-site ions leads to the formation enthalpies of the investigated B-site alloys near the decomposition line. Thus, these alloys will exist as disordered solid solutions at room temperature. For stability, on the one hand, the addition of external elements can cause the stabilizing effect by optimizing the tolerance factor and octahedral factor of halide perovskites; on the other hand, the introduction of impurities can cause the destabilizing effect of [$PbBr_6$] octahedra in the perovskite host lattices. This depends on the difference in ionic radii and electron affinity between the alloying element and Pb, requiring a delicate balance at the specific alloying concentration. The close s, p orbital energies of Pb, Sn, and Ge lead to strong band edge antibonding coupling, which reduces the total energy of Sn and Ge alloys and enhances perovskite stability with the addition of Sn and Ge. The underlying physical mechanism for bandgap tuning by alloying can be attributed to the atomic orbital energy mismatch or quantum confinement effect. This results in significant differences and wide tunability in the bandgap tuning of alloying with different elements. Moreover, compared with Sn and Ge alloys without phase transition, Cd and Mg alloys with cubic-to-hexagonal phase transition show significantly increased electron/hole effective masses. This can be attributed to the fact that the band edge orbital wavefunction in the hexagonal structure does not have 3D spatial continuity, thus, increasing the carrier effective masses and decreasing the electrical transport capacity.

Notably, for the halide perovskite system, although a high alloy ratio can significantly reduce the toxicity of Pb-containing perovskites, a high alloying concentration may also lead to severe distortion of the [MX_6] octahedron because of ionic radius mismatch. The experimental results show that too high alloying ratio may not be conducive to the successful entry of alloying elements to the perovskite lattice but may instead lead to aggregation on the surface of the experimental sample or dissociation in the precursor solution [43-46]. In our work, two specific concentrations, $x = 0.125$ or 0.50, were selected to analyze the effect of B-site alloying on the electronic properties of halide perovskites. The simulation of lower alloying concentrations requires building larger superlattices, particularly for disordered systems, which will undoubtedly cost more computational resources.

The theoretical results of our work at moderate concentrations can still yield accurate trends in thermodynamic stability and electronic structure as a function of concentration x and provide theoretical guidance for further research and development of alloy perovskites with good stability and enhanced optoelectronic properties.

This work was supported by the National Natural Science Foundation of China (Grant Nos. 12004131, and 22090044), and the Jilin Province Science and Technology Development Program (Grant No. 20210508044RQ). Calculations were performed in part at the high-performance computing center of Jilin University.

Supporting Information

The supporting information is available online at http://phys.scichina.com and https://link.springer.com. The supporting materials are published as submitted, without typesetting or editing. The responsibility for scientific accuracy and content remains entirely with the authors.

1 C. C. Stoumpos, C. D. Malliakas, and M. G. Kanatzidis, Inorg. Chem. **52**, 9019 (2013).
2 H. S. Kim, C. R. Lee, J. H. Im, K. B. Lee, T. Moehl, A. Marchioro, S. J. Moon, R. Humphry-Baker, J. H. Yum, J. E. Moser, M. Grätzel, and N. G. Park, Sci. Rep. **2**, 591 (2012).
3 S. D. Stranks, G. E. Eperon, G. Grancini, C. Menelaou, M. J. P. Alcocer, T. Leijtens, L. M. Herz, A. Petrozza, and H. J. Snaith, Science **342**, 341 (2013).
4 X. G. Zhao, J. H. Yang, Y. Fu, D. Yang, Q. Xu, L. Yu, S. H. Wei, and L. Zhang, J. Am. Chem. Soc. **139**, 2630 (2017).
5 X. G. Zhao, D. Yang, Y. Sun, T. Li, L. Zhang, L. Yu, and A. Zunger, J. Am. Chem. Soc. **139**, 6718 (2017).
6 J. S. Manser, M. I. Saidaminov, J. A. Christians, O. M. Bakr, and P. V. Kamat, Acc. Chem. Res. **49**, 330 (2016).
7 M. Mohammadi, S. Gholipour, M. Malekshahi Byranvand, Y. Abdi, N. Taghavinia, and M. Saliba, ACS Appl. Mater. Interfaces **13**, 45455 (2021).
8 X. G. Zhao, D. Yang, J. C. Ren, Y. Sun, Z. Xiao, and L. Zhang, Joule **2**, 1662 (2018).
9 L. Xu, S. Yuan, H. Zeng, and J. Song, Mater. Today Nano **6**, 100036 (2019).
10 T. Li, S. Luo, X. Wang, and L. Zhang, Adv. Mater. **33**, 2008574 (2021).
11 X. Wang, T. Li, B. Xing, M. Faizan, K. Biswas, and L. Zhang, J. Phys. Chem. Lett. **12**, 10532 (2021).
12 Z. Li, M. Yang, J. S. Park, S. H. Wei, J. J. Berry, and K. Zhu, Chem. Mater. **28**, 284 (2016).
13 E. Zheng, Z. Niu, G. A. Tosado, H. Dong, Y. Albrikan, and Q. Yu, J. Phys. Chem. C **124**, 18805 (2020).
14 B. Gao, and J. Meng, Appl. Surf. Sci. **530**, 147240 (2020).
15 X. Wang, J. Yang, X. Wang, M. Faizan, H. Zou, K. Zhou, B. Xing, Y. Fu, and L. Zhang, J. Phys. Chem. Lett. **13**, 5017 (2022).
16 W. J. Mir, M. Jagadeeswararao, S. Das, and A. Nag, ACS Energy Lett. **2**, 537 (2017).
17 A. Sadhanala, S. Ahmad, B. Zhao, N. Giesbrecht, P. M. Pearce, F. Deschler, R. L. Z. Hoye, K. C. Gödel, T. Bein, P. Docampo, S. E. Dutton, M. F. L. De Volder, and R. H. Friend, Nano Lett. **15**, 6095 (2015).
18 I. Levchuk, A. Osvet, X. Tang, M. Brandl, J. D. Perea, F. Hoegl, G. J. Matt, R. Hock, M. Batentschuk, and C. J. Brabec, Nano Lett. **17**, 2765 (2017).
19 Y. Li, G. Na, S. Luo, X. He, and L. Zhang, Acta Phys. Chim. Sin. **37**, 2007015 (2021).
20 A. Swarnkar, W. J. Mir, and A. Nag, ACS Energy Lett. **3**, 286 (2018).
21 C. Eames, J. M. Frost, P. R. F. Barnes, B. C. O'Regan, A. Walsh, and M. S. Islam, Nat. Commun. **6**, 7497 (2015).
22 J. Guo, Y. Fu, M. Lu, X. Zhang, S. V. Kershaw, J. Zhang, S. Luo, Y. Li, W. W. Yu, A. L. Rogach, L. Zhang, and X. Bai, Adv. Sci. **7**, 2000930 (2020).
23 Q. A. Akkerman, D. Meggiolaro, Z. Dang, F. De Angelis, and L. Manna, ACS Energy Lett. **2**, 2183 (2017).
24 A. L. Abdelhady, M. I. Saidaminov, B. Murali, V. Adinolfi, O. Voznyy, K. Katsiev, E. Alarousu, R. Comin, I. Dursun, L. Sinatra, E. H. Sargent, O. F. Mohammed, and O. M. Bakr, J. Phys. Chem. Lett. **7**, 295 (2016).
25 D. Liu, H. Peng, Q. Li, and R. Sa, J. Phys. Chem. Solids **161**, 110413 (2022).
26 C. H. Ri, Y. S. Kim, U. G. Jong, Y. H. Kye, S. H. Ryang, and C. J. Yu, RSC Adv. **11**, 26432 (2021).
27 J. Zhang, Y. Zhong, L. Chen, and L. Yang, Chem. Phys. Lett. **752**, 137572 (2020).
28 R. Sa, B. Luo, Z. Ma, L. Liang, and D. Liu, J. Solid State Chem. **309**, 122956 (2022).
29 A. Walle, and G. Ceder, J. Phase Equil. **23**, 348 (2002).
30 K. Yamamoto, S. Iikubo, J. Yamasaki, Y. Ogomi, and S. Hayase, J. Phys. Chem. C **121**, 27797 (2017).
31 C. Sutton, and S. V. Levchenko, Front. Chem. **8**, 757 (2020).
32 X. T. Wang, Y. H. Fu, G. R. Na, H. D. Li, and L. J. Zhang, Acta Phys. Sin. **68**, 157101 (2019).
33 W. Xiang, Z. Wang, D. J. Kubicki, X. Wang, W. Tress, J. Luo, J. Zhang, A. Hofstetter, L. Zhang, L. Emsley, M. Grätzel, and A. Hagfeldt, Nat. Commun. **10**, 4686 (2019).
34 H. Sato, S. A. Abd. Rahman, Y. Yamada, H. Ishii, and H. Yoshida, Nat. Mater. **21**, 910 (2022).
35 A. Zunger, S. H. Wei, L. G. Ferreira, and J. E. Bernard, Phys. Rev. Lett. **65**, 353 (1990).
36 S. H. Wei, L. G. Ferreira, J. E. Bernard, and A. Zunger, Phys. Rev. B **42**, 9622 (1990).
37 M. M. Tavakoli, S. M. Zakeeruddin, M. Grätzel, and Z. Fan, Adv. Mater. **30**, 1705998 (2018).
38 J. Li, X. Wang, Y. Tan, D. Liang, Y. Zou, L. Cai, T. Wu, K. Wen, Y. Wang, Y. Li, T. Song, L. Wang, and B. Sun, Adv. Opt. Mater. **8**, 2001073 (2020).
39 A. Goyal, S. McKechnie, D. Pashov, W. Tumas, M. van Schilfgaarde, and V. Stevanović, Chem. Mater. **30**, 3920 (2018).
40 J. C. Blancon, A. V. Stier, H. Tsai, W. Nie, C. C. Stoumpos, B. Traoré, L. Pedesseau, M. Kepenekian, F. Katsutani, G. T. Noe, J. Kono, S. Tretiak, S. A. Crooker, C. Katan, M. G. Kanatzidis, J. J. Crochet, J. Even, and A. D. Mohite, Nat. Commun. **9**, 2254 (2018).
41 K. J. Lee, B. Turedi, L. Sinatra, A. A. Zhumekenov, P. Maity, I. Dursun, R. Naphade, N. Merdad, A. Alsalloum, S. Oh, N. Wehbe, M. N. Hedhili, C. H. Kang, R. C. Subedi, N. Cho, J. S. Kim, B. S. Ooi, O. F. Mohammed, and O. M. Bakr, Nano Lett. **19**, 3535 (2019).
42 Y. Jiang, C. Qin, M. Cui, T. He, K. Liu, Y. Huang, M. Luo, L. Zhang, H. Xu, S. Li, J. Wei, Z. Liu, H. Wang, G. H. Kim, M. Yuan, and J. Chen, Nat. Commun. **10**, 1868 (2019).
43 J. K. Chen, J. P. Ma, S. Q. Guo, Y. M. Chen, Q. Zhao, B. B. Zhang, Z. Y. Li, Y. Zhou, J. Hou, Y. Kuroiwa, C. Moriyoshi, O. M. Bakr, J. Zhang, and H. T. Sun, Chem. Mater. **31**, 3974 (2019).
44 N. Phung, R. Félix, D. Meggiolaro, A. Al-Ashouri, G. Sousa e Silva, C. Hartmann, J. Hidalgo, H. Köbler, E. Mosconi, B. Lai, R. Gunder, M. Li, K. L. Wang, Z. K. Wang, K. Nie, E. Handick, R. G. Wilks, J. A. Marquez, B. Rech, T. Unold, J. P. Correa-Baena, S. Albrecht, F. De Angelis, M. Bär, and A. Abate, J. Am. Chem. Soc. **142**, 2364 (2020).
45 X. Zhang, X. Ren, B. Liu, R. Munir, X. Zhu, D. Yang, J. Li, Y. Liu, D. M. Smilgies, R. Li, Z. Yang, T. Niu, X. Wang, A. Amassian, K. Zhao, and S. F. Liu, Energy Environ. Sci. **10**, 2095 (2017).
46 R. Zeng, L. Zhang, Y. Xue, B. Ke, Z. Zhao, D. Huang, Q. Wei, W. Zhou, and B. Zou, J. Phys. Chem. Lett. **11**, 2053 (2020).